

Chemical etching enhanced nanosecond pulsed laser micromachining: An experimental and numerical investigation

Fazlay Rubbi^b, Xing Zhang^{a,*}, Fatemeh Delzendehrooy^b, Bo Mao^c, Qiong Nian^d, Charalabos C. Doumanidis^e, Yiliang Liao^{b,*}

^a School of Mechanical and Electrical Engineering, Soochow University, Suzhou, Jiangsu 215100, China

^b Department of Industrial and Manufacturing Systems Engineering, Iowa State University, Ames, IA 50011, USA

^c School of Materials Science and Engineering, Shanghai Jiao Tong University, Shanghai 200240, China

^d School of Engineering for Matter, Transport and Energy, Arizona State University, Tempe, AZ 85287, USA

^e W.B. Burnsed Jr. Dept of Mechanical, Aerospace and Biomedical Engineering, University of South Alabama, Mobile, AL 36688, USA

ARTICLE INFO

Keywords:

Pulsed laser micromachining
Laser ablation
Chemical etching
Modeling

ABSTRACT

Nanosecond pulsed laser micromachining (PLM) under liquid confinement is a highly precise, flexible, efficient, and non-contact manufacturing process being used in widespread applications. The process efficiency of the PLM as determined by the laser ablation rate, however, often quickly reaches saturation with the increase of laser energy. This is ascribed to the screening effect of laser-induced plasma that absorbs part of incident energy. In this study, a chemical etching enhanced PLM (CE-PLM) is developed to tackle this challenge. By replacing water (H₂O) with an environmentally friendly and active liquid confinement - hydrogen peroxide (H₂O₂), single-shot laser ablation experiments were firstly performed on different metallic materials to evaluate the considerably enhanced ablation rate. Then, the beneficial effects of H₂O₂ on PLM applications including micro-drilling and micro-grooving were investigated. The enhanced ablation rate and PLM efficiency were attributed to the synergistic effect of laser ablation and ultrafast chemical etching. Moreover, a physics-based model was developed to elucidate the process mechanism, with focus on revealing the contribution of chemical etching to the material removal during CE-PLM as affected by laser processing parameters. The findings of this study will contribute to enhancing the efficiency and capability of PLM techniques towards broader industrial applications.

1. Introduction

Due to its high precision, good flexibility, and fast processing speed, pulsed laser micromachining (PLM) has been widely used in industrial applications (e.g., micro-drilling, micro-grooving, micro-texturing) to produce micro-/nano-features [1–6]. These PLM applications typically involve the removal of material through the ablation process during which the target material is vaporized due to the laser-matter interactions [7]. As a result, the process efficiency of PLM is strongly governed by the laser ablation rate, and research efforts have been put into boosting up the ablation rate for improved process efficiency towards extended applications. In recent years, introducing liquid confining media such as water (H₂O) has been proven to be an effective method to enhance the PLM process efficiency [8–12] due to the promoted ablation rate. In detail, during the non-confined PLM process, the interactions between the laser and the target material give rise to the

generation of laser-induced plasma (LIP) that expands into the free space. However, in the case where the target material is immersed in a transparent liquid medium, the hydrodynamic expansion of the LIP is confined due to the presence of the surrounding liquid environment [13–15], leading to significant increases in the plasma temperature and pressure [16,17]. Consequently, such confining effect could result in considerably enhanced ablation rate, which has been reported by several research groups [8,9,18]. For instance, Zhu et al. [8] conducted a comparative analysis of laser ablation of silicon in air and H₂O, demonstrating an ablation rate of 0.07 μm/pulse in H₂O while only 0.03 μm/pulse in air. Lv et al. [9] reported a similar observation, where the ablation depth on an Inconel 718 surface at a pulse energy of 12 mJ was substantially increased by 167% from 27 to 72 μm when applying H₂O as the confinement instead of processing in the open air.

Despite existing efforts, the current PLM process under the liquid confinement still encounters a significant limitation: when the laser

* Corresponding authors.

E-mail addresses: xingzhang@suda.edu.cn (X. Zhang), leonl@iastate.edu (Y. Liao).

<https://doi.org/10.1016/j.jmapro.2023.11.017>

Received 6 July 2023; Received in revised form 19 October 2023; Accepted 6 November 2023

Available online 11 November 2023

1526-6125/© 2023 The Society of Manufacturing Engineers. Published by Elsevier Ltd. All rights reserved.

intensity surpasses a critical threshold, the breakdown of liquid confinement leads to the formation of a secondary plasma, impeding the transmission of incident laser energy [19–22]. Consequently, this breakdown phenomenon causes a saturation in the ablation rate, thereby limiting the capabilities and efficiency of PLM. Berthe et al. [21] investigated the transmission of the H_2O breakdown plasma as affected by laser intensity during the laser ablation process. It was found that the energy transmission cut-off occurred at a laser intensity of 6 GW/cm^2 , and the saturation effect was found at 10 GW/cm^2 . Such saturation phenomenon was also reported by Lopez et al. [23] in their research on the micro-drilling of tungsten carbide blocks. A linear relationship was observed between the ablation rate and the laser energy, but the rate reached a maximum value of $0.5 \mu\text{m/pulse}$ once the laser fluence exceeded 5 J/cm^2 . Shiby et al. [24] found that the LIP shielding phenomenon even caused a decrease in ablation rate during the micro-scribing of copper films when the laser energy exceeded a threshold of approximately 18 J/cm^2 with a laser pulse width of 6 ns. Therefore, it is of specific technical interest to explore other potential strategies for improving the efficiency of PLM processes.

Chemical etching, as an alternative approach of micromachining, can effectively remove the material by chemical reaction at the etchant/target interface [25–27]. Accordingly, a process design aiming to integrate laser ablation with chemical etching could greatly enhance the PLM efficiency, which has been demonstrated by previous research work [28–30]. However, the utilization of acid/alkali-based liquids (e.g., HF, HCl, and HNO_3) in these work challenges in controlling the ablation rate and maintaining the desired surface feature quality due to the aggressive etching reaction that may occur even at room temperature. In addition, these strong etchants can cause adverse environmental impacts. Consequently, PLM under strong etchants has not been widely used in industrial scenes. Thus, it is of great importance to examine the efficacy of PLM in an environmentally friendly and relatively mild etchant.

In this paper, we investigate a high-efficiency and environmentally friendly chemical etching enhanced PLM (CE-PLM) process, during which the laser ablation is performed under an active liquid confinement - hydrogen peroxide (H_2O_2), leading to the significantly enhanced material removal rate. Firstly, single-shot laser ablation experiments with liquid confinement of H_2O_2 were firstly conducted on various metallic materials including zinc (Zn), aluminum (Al), and copper (Cu). Then, the beneficial effects of H_2O_2 on practical PLM applications including micro-drilling and micro-grooving were further demonstrated. Lastly, to advance the fundamental understanding of process mechanism, a physics-based model incorporating both evaporative ablation and chemical reaction was established. The as-produced feature profiles and depths at different experimental conditions were simulated and compared with experimental measurements. We envision that the CE-PLM can be applied to enhance the process efficiency and capability of a variety of PLM techniques towards widespread industrial applications.

2. Methods

2.1. Experimental configuration

The experimental configuration of the CE-PLM experiment is illustrated in Fig. 1. A Surelite III Q-switched Nd-YAG laser (Amplitude Laser Inc.) emitting laser pulses with a maximum energy of 850 mJ, a wavelength of 1064 nm and a pulse duration of 5 ns was employed. The laser beam was directed towards the sample surface via three reflective mirrors and a focus lens with a focal distance of 200 mm. The sample was submerged in a container partially filled with H_2O_2 (30% aq.) solution, which is affixed to XY linear stages. The thickness of the liquid layer over the sample surface was selected based on literature regarding underwater laser-based micromachining processes. Typically, a layer thickness ranging from 0.5 to 10 mm was used in the literature [18,31,32]. In our case, the thickness of the liquid layer over the sample surface was optimized to be 5 mm, to prevent the occurrence of water

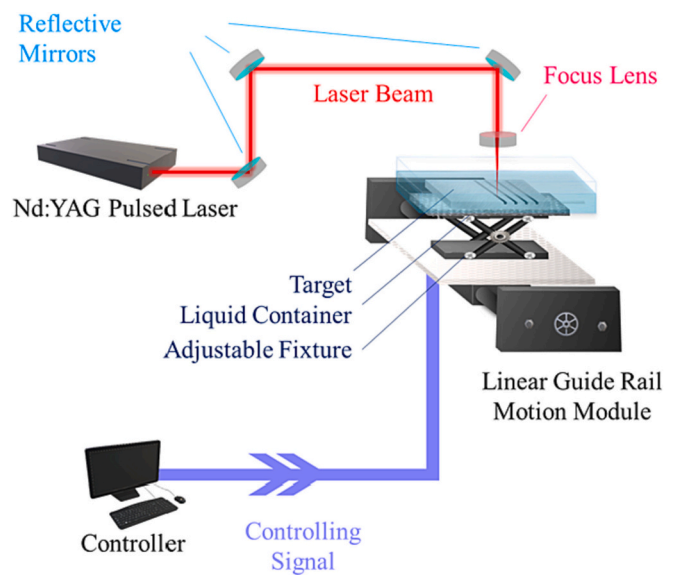


Fig. 1. The schematic illustration of CE-PLM experimental setup.

splashing with a thin liquid layer or the substantial loss of incident energy absorbed by a thick liquid layer. Firstly, pure Zn, Cu and Al blocks (McMaster-Carr) with the same size of $20 \times 10 \times 6 \text{ mm}^3$ were used as the target materials for single-shot laser ablation experiments. Prior to ablation experiments, the samples were ground using 1200-grit silicon carbide sandpaper. After laser processing, the samples were rinsed with deionized water, followed by drying using compressed air. The ablated crater was characterized by an R-Tech profilometer, and the results were analyzed by Gwyddion software. Then, Al sheets were employed for the micro-drilling and micro-grooving experiments. For the micro-drilling, the laser intensity varying from 3 to 7 GW/cm^2 and a pulse frequency of 10 Hz were utilized. A Leica DM18-A optical microscope (OM) was employed to measure the diameter of the drilled micro-holes and a FEI INSPECT F50 scanning electron microscopy (SEM) was employed to examine the cross-sectional geometry of micro-holes. For the multi-scan micro-grooving, the experiments were performed with different scanning times ranging from 10 to 200 at a laser intensity of 7 GW/cm^2 , a pulse frequency of 10 Hz, and a scanning speed of 2.5 mm/s. The surface morphologies of micro-grooves were examined by SEM and the groove depth was measured by OM from the cross-sectional view. PLM under H_2O (w-PLM) was also carried out with the same setup for comparison.

2.2. Numerical simulation

2.2.1. Single-shot laser ablation

To gain a better understanding of the proposed CE-PLM process and predict the ablation rate, a physics-based model was established. In this regard, the following governing partial differential equations were solved numerically using the explicit finite difference method (FDM). The source code for the numerical simulation was implemented in MATLAB software. To preserve the accuracy of the model and guarantee the convergency of the solution, by performing sensitivity analysis, the temporal and spatial step size were fixed on $\Delta t = 1^{-12} \text{ s}$ and $\Delta z = 1^{-10} \text{ m}$, respectively. During the PLM process, the laser beam diameter is often considerably larger than the optical penetration depth. Therefore, the energy absorbed by the target material can be considered as one dimensional problem, and the temperature distribution as a function of the target depth $T(t, z)$ can be formulated by [33–35]:

$$\rho c \frac{\partial T}{\partial t} = \frac{\partial}{\partial z} \left(k \frac{\partial T}{\partial z} \right) + \alpha(1-R)A_c I(t) e^{-\alpha z} + \Delta E_T \quad (1)$$

where R and α denote the material reflectivity and absorption

coefficient, respectively. ρ , C and k represent the density, temperature-dependent specific heat capacity and thermal conductivity of the target material, respectively. A_c is the transmissivity of the liquid confinement to the laser. ΔE_T is the thermal energy released during etching process and is expressed by $\Delta E_T = V(t)E_v$, where $V(t)$ is the chemical-participated volume and E_v is the released volumetric thermal energy. $I(t)$ represents laser intensity for a Gaussian beam pulse as a function of time and can be calculated by [36,37]:

$$I(t) = \frac{2}{\sqrt{\pi/\ln 2}} I_{PLA} \text{Exp} \left[-\frac{(t - \mu_d)^2}{2\sigma^2} \right] \quad (2)$$

where I_{PLA} is the peak intensity of the laser beam, μ_d is the delay time, and σ is the pulse standard deviation related to pulse duration τ_L by $\tau_L = 2\sqrt{2\ln 2}\sigma$.

To determine the material removal due to the vaporization during laser-matter interactions, the Hertz-Knudsen [38] and Clausius-Clapeyron equations are implemented. Accordingly, the evaporation contributes to the recession of the irradiated surface, and the recession velocity v_a can be computed by [39]:

$$v_a = 0.82 \frac{p_0}{\rho} \frac{\sqrt{M}}{\sqrt{2\pi k_B T_s}} \text{exp} \left[\frac{MH_v(T_b)}{k_B} \left(\frac{1}{T_b} - \frac{1}{T_s} \right) \right] \quad (3)$$

where M is the atomic mass of the target material, and k_B is the Boltzmann constant. T_s is the surface temperature, and T_b is the normal boiling point. $H_v(T_b)$ is the latent heat of vaporization, and $p_0 = 1.013 \times 10^5$ Pa is the standard atmospheric pressure. Accordingly, the evaporative ablation depth h_{vap} under a single laser pulse can be computed by integrating the recession velocity over time [40]:

$$h_{vap} = \int_0^{\tau_I} v_a dt \quad (4)$$

where τ_I is the thermal relaxation time corresponding to temperatures above T_b . To obtain the evaporative ablation depth h_{vap} , the top and bottom boundary conditions are incorporated in the thermal model:

$$-k \frac{\partial T}{\partial z} \Big|_{z=0} = -\rho v_a H_v(T_b) - h(T_s - T_{amb}), \quad \frac{\partial T}{\partial z} \Big|_{z=L} = 0 \quad (5)$$

where h is the convective coefficient of liquid confinement, and T_{amb} is the ambient temperature which is set to be the initial temperature $T(z, t = 0) = 300$ K.

In this study, due to the existence of liquid confinement, the hydrodynamic expansion of LIP is confined within tens of ns [41]. Thus, to achieve a simplified model, it is postulated that the decomposition of H_2O_2 primarily takes place at the liquid-metal interface, where the laser-matter interactions give rise to the high-temperature vapor/plasma plume. According to Hong et al. [42], the decomposition rate of H_2O_2 at elevated temperatures (above 1000 K), k_r , exhibits a magnitude on the order of $10^8 \text{ cm}^3 \text{ mol}^{-1} \text{ s}^{-1}$. Hence, volume $V(t)$ of H_2O_2 associated with the ultrafast chemical reaction can be approximated by:

$$V(t) = \int_0^{\tau_{II}} \int_0^{h_{vap}} \pi r^2 c_r k_r dz_{vap} dt \quad (6)$$

where τ_{II} is the thermal relaxation time corresponding to temperatures above 1000 K, c_r is the concentration of H_2O_2 . The profile of the evaporation-induced ablated region can be expressed by $z_{vap} = h_{vap} \text{exp}(-2r^2/w^2)$, where h_{vap} is the evaporation depth. The total material removal depth incorporating both evaporative ablation and etching reaction can be given as $z_m = h_m \text{exp}(-2r^2/w^2)$, where h_m can be computed by solving the integral equation that describes the chemical etching reaction-participated volume:

$$\int_0^{\tau_{II}} \int_0^{h_{vap}} \pi r^2 c_r k_r dz_{vap} dt = \int_0^{h_m} \pi r^2 dz_m - \int_0^{h_{vap}} \pi r^2 dz_{vap} \quad (7)$$

The modeling results will be compared with experimental findings in the case of CE-PLM of Zn, and the material parameters used for Zn in the current modeling are shown in Table 1.

2.2.2. Multi-shot PLM process

In multi-shot PLM experiments, the material removal and reduction in target thickness lead to an increase in the distance between the focal plane of the laser beam and the target surface. Meanwhile, the melt ejection due to recoil pressure causes an increase in the effective area on the material surface irradiated by the laser beam. These changes in geometrical characteristics cause a decrease in the laser intensity as the PLM proceeds. To incorporate this phenomenon in our work, the numerical photo-thermal model proposed by Stafe et al. [48,49] is employed. The model utilizes Clausius-Clapeyron equation to calculate the saturated vapor pressure, which is influenced by the recoil pressure generated during evaporation. This recoil pressure exerts a force on the molten surface, expelling the melt layer from the ablated region and causes an increase in the rim height around the crater [49]. The thickness (h_{melt}) of the melt layer can be defined as the depth where temperature exceeds the melting temperature of the target material. By applying Bernoulli hydrodynamic equation, the average velocity of the melt can be determined by [48]:

$$v_m = \sqrt{\frac{2(\Delta p - \rho_l g h_{cr})}{\rho_l}} \quad (8)$$

where ρ_l , g , and h_{cr} are liquid density, gravity, and crater depth, respectively. $\Delta p = p_{rec} - p_0$ is the difference between recoil pressure and pressure outside of laser spot. Furthermore, based on the continuity equation, an approximation of the normal ejection velocity of each point located on the receded target surface can be expressed as [48]:

$$v_{ej} = \left(\frac{A_0}{A_c} \right) v_m \quad (9)$$

where $A_0 = 2\pi r h_{melt}$ is the cylindrical lateral area around the crater generated by piston action of irradiated surface. A_c represents the incident area of laser beam, with the lateral surface of crater considered as paraboloid of radius r and crater height h_c . Considering the continuity equation and the recession of the melt front, the increase in the radius of the crater can be estimated by integrating the ejection velocity over time [48]:

$$\Delta h_{ej} = \int_0^{\tau_I} v_{ej} dt \quad (10)$$

The flowchart describing the proposed numerical simulation is presented in Fig. 2. The PLM process model initiates by considering input parameters including laser energy, thermophysical properties, and the number of laser shots. Note that the beam kinematics must be updated at each iteration cycle, to account for the increased beam radius and area exposed to the laser input. The initial temperature chosen at the

Table 1
Material parameters used for modeling CE-PLM of Zn and Al [43–48].

Property	Nomenclature	Value for Zn (units)	Value for Al (units)
Density	ρ	7.14 (g/cm ³)	2.71 (g/cm ³)
Specific heat capacity	c	0.39 (J/g/K)	0.91 (J/g/K)
Thermal conductivity	k	117 (W/m/K)	215 (W/m/K)
Reflectivity	R	0.575	0.815
Absorption coefficient	α	4.1×10^7 (m ⁻¹)	7.5×10^7 (m ⁻¹)
Boiling point	T_b	1180 (K)	2730 (K)
Melting Temperature	T_m	692.7 (K)	930 (K)
Transmissivity of confinement	A_c	83%	83%
Latent heat of vaporization	H_v	1.78×10^6 (kJ/kg)	1.09×10^7 (kJ/kg)

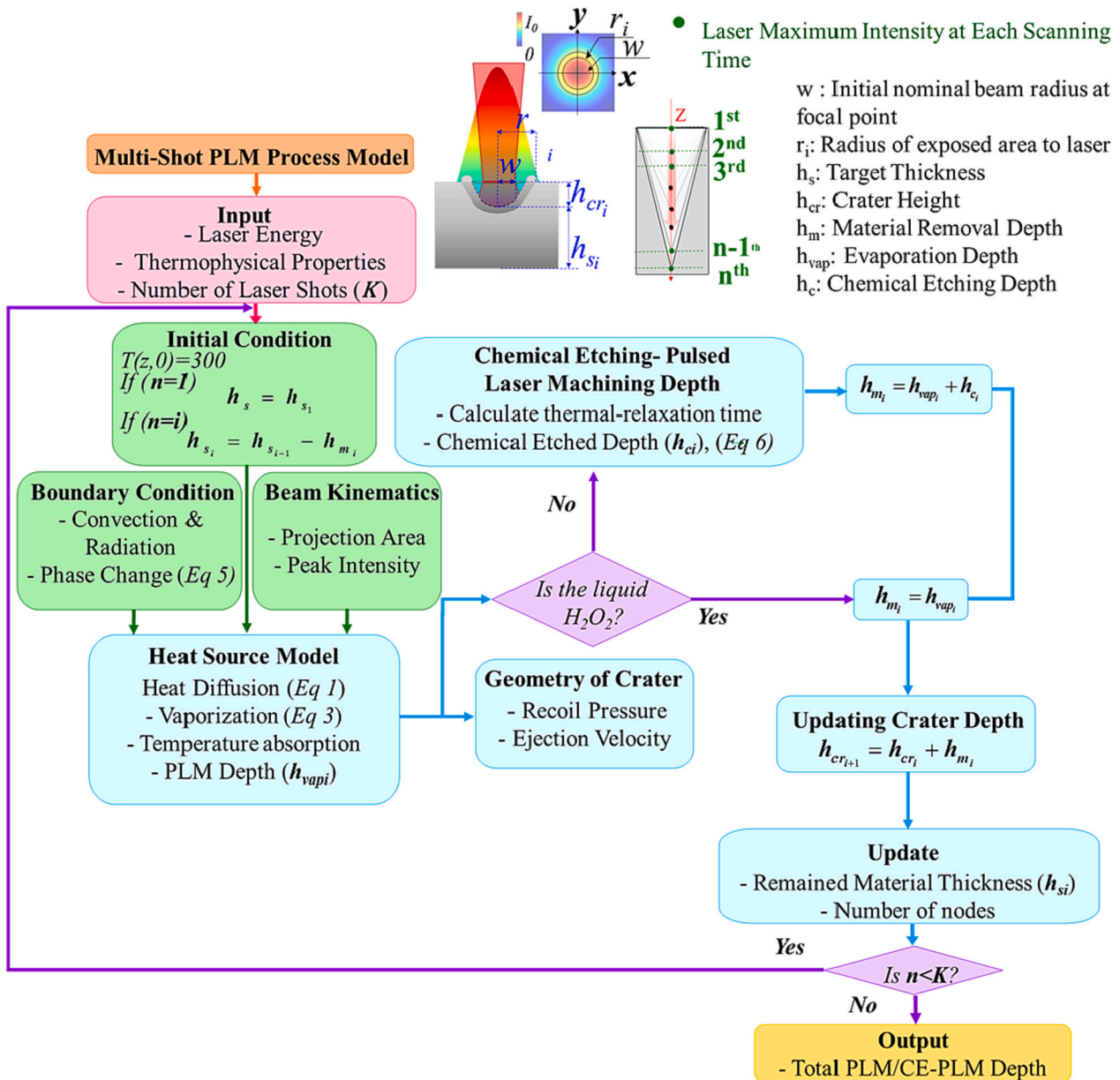


Fig. 2. Flowchart of multi-shot CE-PLM simulation.

beginning of each laser shot can be considered as the ambient temperature. This assumption is derived from the consideration that the heat accumulation is negligible between adjacent cycles, since the thermal relaxation time is considerably shorter than the time gap between two consecutive laser shots [48]. The initial settings, boundary conditions, and beam kinematics are executed within the heat source model to determine the evaporation-induced ablation depth (h_{vap}) after each laser shots. The output from the heat source model is then utilized to calculate the recoil pressure and ejection velocity, facilitating the estimation of crater geometry. Additional calculations of thermal relaxation time (τ_{II}) and etching-induced material removal depth (h_c) are performed, yielding the total material removal depth (h_m). This calculation enables the updating of the target material thickness and the number of nodes at each simulation step. To maintain a consistent spatial step size, the number of nodes corresponding to the material removal depth after each cycle is calculated, and the total number of nodes is recalibrated at the beginning of subsequent laser shot. This meticulous consideration maintains mesh sensitivity in problem-solving and ensures accurate thermal distribution in each time step. The iteration ends until the

simulation steps reach the desired number of cycles K . The established model will be validated by experimental data in the case of micro-grooving of Al, and the employed material parameters are listed in Table 1.

3. Results and discussion

3.1. Experimental results

Prior to PLM applications, single-shot laser ablation experiments were performed on different materials to examine the effect of active liquid confinement on the ablation rate. Fig. 3(a-c) and 3(d-f) show the two-dimensional optical images of the ablated crater produced on the Zn, Al, and Cu surfaces by laser ablation under H_2O and H_2O_2 confining media, respectively. Note that each ablated crater was produced by five laser pulses to minimize the error caused by the variation in pulse energy. The extracted cross-sectional profiles of craters were presented in Fig. 3(g-i), indicating the influence of different confining media on the geometrical characteristics of ablation region. It is found that laser

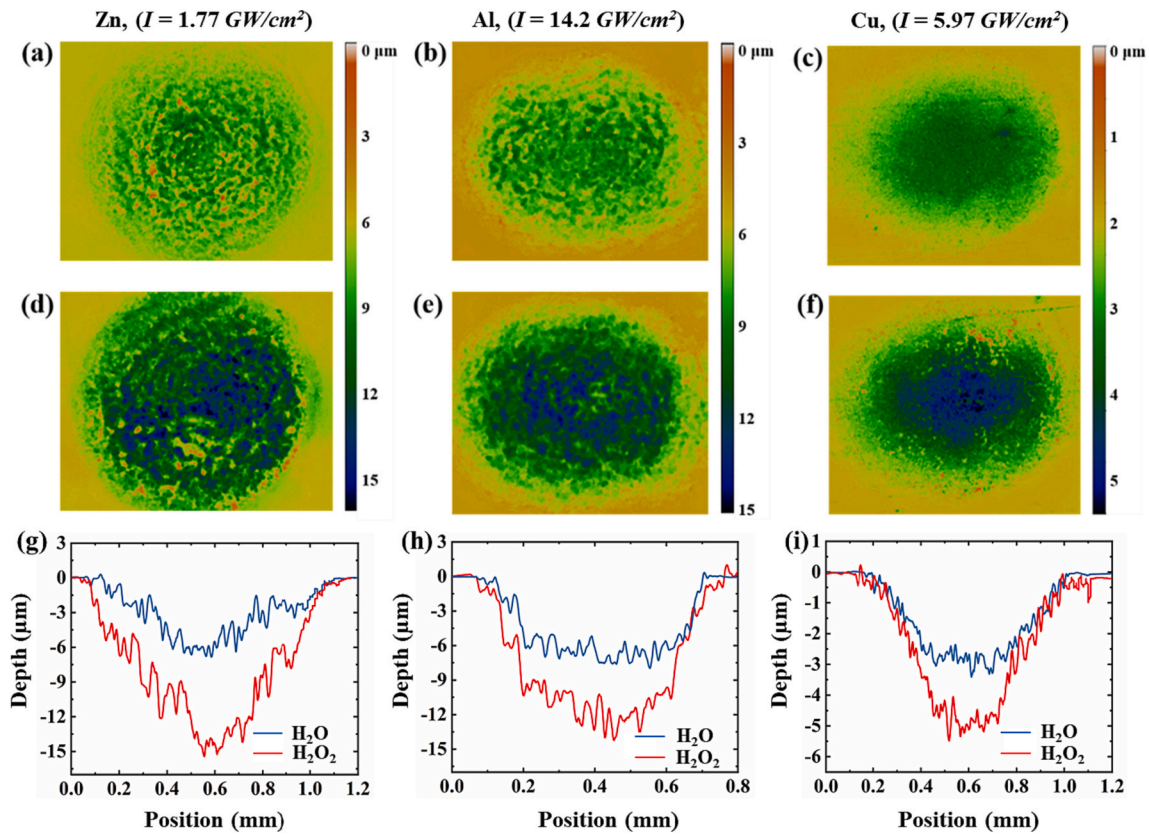


Fig. 3. Optical images of the ablated craters produced by laser ablation under (a-c) H₂O and (d-f) H₂O₂, and (g-i) the comparison of cross-sectional profiles of the ablated craters. The target materials and applied laser intensities are: (a, d, g) Zn samples under a laser intensity of 1.77 GW/cm², (b, e, h) Al samples under a laser intensity of 14.2 GW/cm², and (c, f, i) Cu samples under a laser intensity of 5.97 GW/cm².

ablation under H₂O₂ results in a greater ablation depth for all three materials compared to laser ablation under H₂O. For instance, the maximum depth of the ablated crater on Zn surface at a laser intensity of 1.77 GW/cm² is increased by 155% from 5.8 to 14.8 μm when utilizing H₂O₂ as the liquid confinement instead of H₂O. In addition, the crater diameter is increased by approximately 10% from 1 to 1.1 mm. Similar enhancements are also observed for the cases of Al and Cu samples, where the ablation depths are increased by 90.2% from 7.2 to 13.7 μm and 51.5% from 3.3 to 5 μm, respectively. These experimental results prove that replacing H₂O with an active liquid confinement such as H₂O₂ can significantly increase the laser ablation rate.

To further study the enhancement of laser ablation rate by active liquid confinement, a series of experiments on different materials were performed under H₂O and H₂O₂ with various laser intensities. By comparing the experimental results of Zn samples [Fig. 4(a)], it is found that the ablation depth is increased at all laser intensities by utilizing H₂O₂ as the confinement instead of H₂O, e.g., from 3.3 to 8.2 μm at 1.32 GW/cm², and from 7.5 to 20.2 μm at 2.20 GW/cm². Moreover, such enhancement in the ablation rate becomes increasingly prominent as the laser intensity increases. For example, the crater depth is increased by 67% at 0.53 GW/cm², 125% at 0.88 GW/cm², and 148% at 1.32 GW/cm². This could be caused by the enlarged ablation region and prolonged thermal relaxation time at higher laser intensities, leading to a larger amount of H₂O₂ participating in the chemical reactions. The experimental results of Al [Fig. 4(b)] and Cu [Fig. 4(c)] samples present similar observations. It is noteworthy that the ablation depth in the cases under H₂O reaches a saturation point once the laser intensity reaches a certain threshold value (e.g., 11 GW/cm² for Cu) because of the LIP screening the laser energy from irradiating the target material. Near such threshold value, the ablation rate is significantly improved when replacing H₂O with H₂O₂ [Fig. 4(d)]. To be specific, the ablation rate is

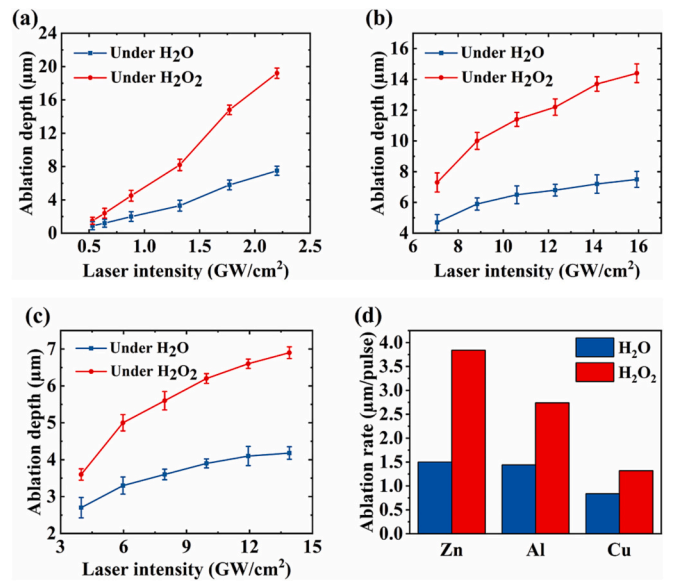


Fig. 4. Ablation depths of (a) Zn, (b) Al, (c) Cu samples as affected by the laser intensity. (d) Ablation rates for Zn (at 2.20 GW/cm²), Al (at 14.15 GW/cm²) and Cu (at 11.94 GW/cm²).

enhanced by 156% from 1.50 to 3.84 μm/pulse for Zn at 2.20 GW/cm², 90.2% from 1.44 to 2.74 μm/pulse for Al at 14.15 GW/cm², and 57% from 0.84 to 1.32 μm/pulse for Cu at 11.94 GW/cm². More importantly, when exceeding the threshold value, the ablation depth in the cases under H₂O₂ still increases at a slow rate with increasing the laser

intensity. It is, thus, demonstrated that the integration of laser ablation and chemical etching can serve as an effective strategy to break the major limitation induced by confinement breakdown in conventional laser ablation under H₂O.

Next, the proposed approach was applied to practical PLM applications including micro-drilling and micro-grooving. Fig. 5 presents the results of through-hole micro-drilling under H₂O and H₂O₂ on the 1-mm-thick Al sheet at varying laser intensities. It is observed that the pulse number required to produce a through-hole is significantly reduced when replacing H₂O with H₂O₂ as the confinement, as depicted in Fig. 5 (a). For example, given a laser intensity of 7 GW/cm², it takes 3000 pulses to drill the through-hole under H₂O whereas only 417 pulses under H₂O₂. To quantitatively assess the enhanced drilling efficiency, we define such enhancement due to active liquid confinement by $\eta = N_{H_2O_2}/N_{H_2O}$, where N is the required number of laser pulses to drill the through-hole. It is found that the enhancement in the drilling efficiency generally increases with increasing the laser intensity. For example, the micro-drilling efficiency is enhanced by a factor of 5.37 at 3 GW/cm² and by a factor of 7.42 at 7 GW/cm². This is consistent with our single-shot laser ablation experiments shown in Fig. 4. Fig. 5(b-e) represents the morphologies of the drilled micro-holes on the Al target under H₂O and H₂O₂ at 7 GW/cm². The images exhibit similar surface morphology except that the entrance diameter of the micro-holes produced under H₂O₂ is ~25 μ m larger than that under H₂O. According to the cross-sectional view of through-holes, it can be calculated that replacing H₂O with H₂O₂ during through-hole micro-drilling leads to approximately 10% higher volume of material removal.

Figs. 6 and 7 present the results of micro-grooving under H₂O and H₂O₂ on the Al sheet with different laser scanning times (ranging from 10 to 200) at a constant laser intensity of 7 GW/cm². It can be found in Fig. 6 that the depth of micro-grooves increases exponentially with increasing the scanning times under both confinements, and the depth of micro-grooves produced by CE-PLM is larger than that produced by w-PLM. For instance, given a scanning-times of 100, the groove depth reaches 168 μ m under H₂O₂ while only 91 μ m under H₂O. In addition, it is noted that such increase in groove depth could be reduced at higher scanning times. For example, the depth increases by 83.3% from 42 to 77 μ m at the scanning times of 50, whereas by 62.8% from 191 to 311 μ m at the scanning times of 200. This phenomenon can be explained by the continuous decrease in laser intensity as PLM proceeds, as described in Section 2.2.2. Overall speaking, these experimental findings confirm that the proposed CE-PLM process is an effective strategy to enhance the PLM efficiency.

The impacts of confining media on the surface morphologies of micro-grooves were also examined, as revealed in Fig. 7(a-d). The groove width (indicated by orange markings) was evaluated by averaging the measurements taken at five different locations within each

micro-groove. The results demonstrate that micro-grooves become slightly wider and smoother (less wrinkled) with increasing the scanning times. The smoothing phenomenon observed in this study was also observed in other work [50]. At the initial stage of multi-scan processing, the spatters induced by the laser-matter interactions could form on the micro-groove surface, leading to the rough groove surface. During subsequent scanning processing, the micro-groove becomes smoother due to the re-ablation effect exerted on the pre-existing spatters. Fig. 7(e-h) presents the micro-grooves produced by CE-PLM under H₂O₂, also showing smoothing phenomenon as the scanning times increases. However, given the constant scanning times, the micro-groove produced by CE-PLM exhibits a smoother morphology than that by w-PLM, which could be ascribed to the removal of spatters by the dynamic etching reactions under H₂O₂.

The mechanism elucidating the significantly enhanced processing efficiency of PLM by replacing H₂O with H₂O₂ is proposed and schematically illustrated in Fig. 8. When the front part of a high-energy ($h\nu$) laser beam is irradiated onto the material surface, the target material is immediately vaporized and even ionized because of the rising temperature, inducing the formation of a laser-induced vapor/plasma plume. Such ionization process is dominated by the inverse-bremsstrahlung mechanism, which is associated with the rapid increase in the number of free electrons (e^-) [Eq. (a)]. Once the plume is generated at the metal-liquid interface, it provides an ideal high-temperature (several thousand Kelvin) environment for the rapid decomposition of liquid confinement (H₂O₂), releasing the atomic oxygen (O) as a strong oxidizer for the local etching reactions [Eq. (b)]. It is worth noting that these released atomic oxygen could be confined at the interface due to the presence of liquid confinement. Moreover, a portion of the released atomic oxygen may undergo further ionization by absorbing subsequent laser energy, contributing to the formation of ionized oxygen (O⁺) as a stronger oxidizer through the inverse-bremsstrahlung process [51]. Consequently, a thin layer of plume consisting of high-concentrated strong oxidizers (O and O⁺) is formed at the metal-liquid interface, leading to an ultrafast chemical etching process that efficiently removes a greater amount of target material [Eq. (c)]. Furthermore, the thermal energy (ΔE_T) released during the chemical etching process could induce a further elevation of the plume temperature that benefits the material removal rate. Thus, a synergistic relationship is achieved between the evaporative ablation and chemical etching reaction, leading to the higher material removal rate during CE-PLM in comparison with the conventional w-PLM.

3.2. Numerical results

To comprehensively understand the role of ultrafast chemical etching on material removal during CE-PLM, a physics-based modeling

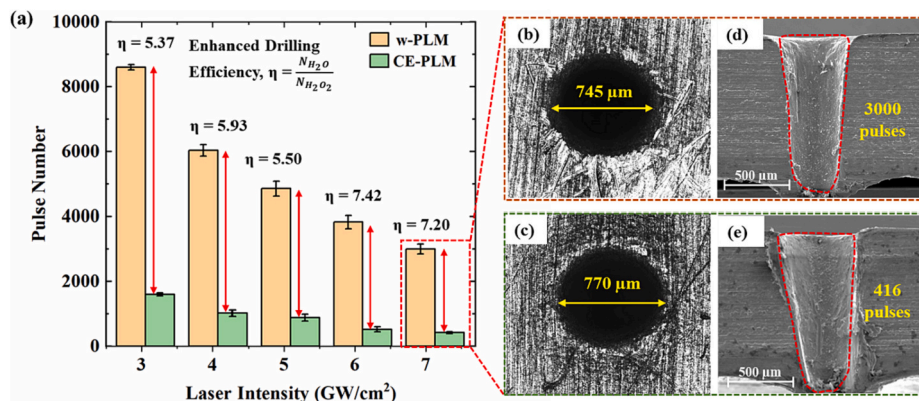


Fig. 5. (a) Enhanced micro-drilling efficiency at different laser intensities for pure Al. (b-e) Morphologies of micro-holes drilled under H₂O (b, d) and H₂O₂ (c, e) at a laser intensity of 7 GW/cm².

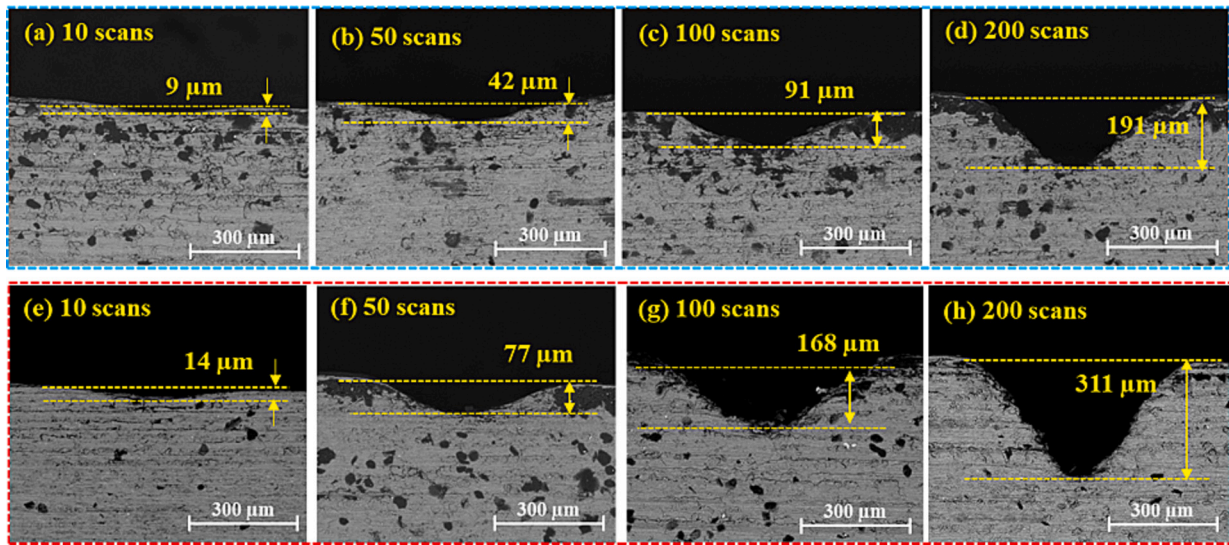


Fig. 6. Cross-sectional SEM images of the microgrooves on the Al sheet under (a-d) H₂O and (e-h) H₂O₂ at 10, 50, 100 and 200 scanning times and a fixed laser intensity of 7 GW/cm².

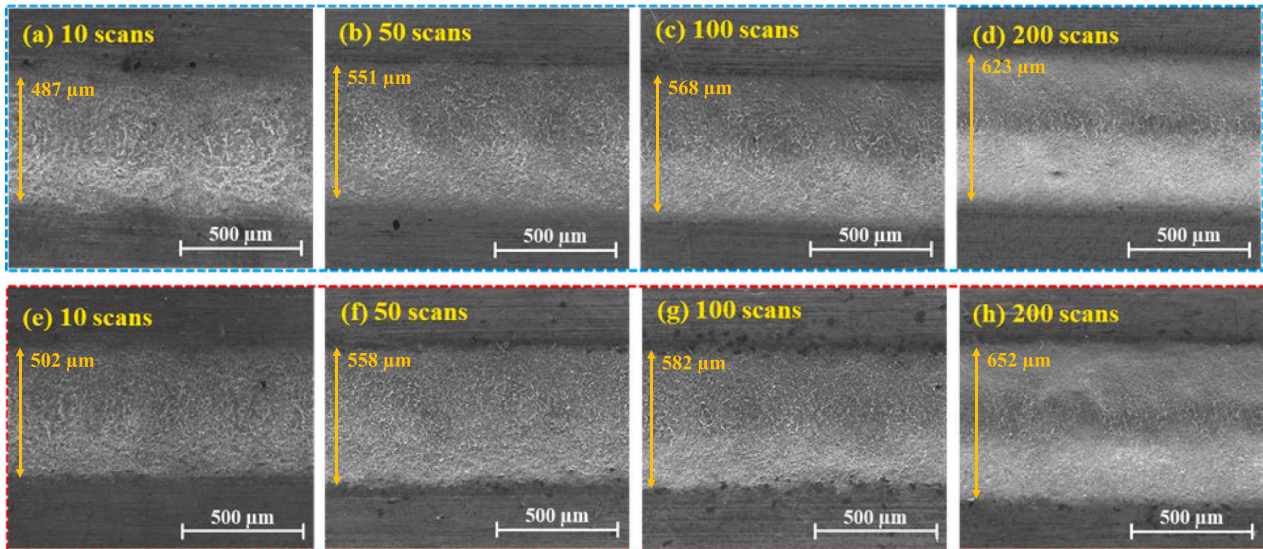


Fig. 7. Top-view SEM images of the micro-grooves on the Al sheet under (a-d) H₂O and (e-h) H₂O₂ with varying scanning times at a fixed intensity of 7 GW/cm².

(Section 2.2) is performed to elucidate the aforementioned process mechanism. In the following discussion, the modeling effort is conducted to firstly investigate the laser-induced high-temperature conditions for evaporation and chemical reaction. Then, the major effort is put into investigating the contribution of chemical etching to the material removal during CE-PLM as affected by processing parameters. Given a laser intensity of 7 GW/cm², a pulse duration of 5 ns, and a delay time of 12.5 ns, the contour plots of the simulated temperature evolution as a function of depth and time for the laser ablation of Al is shown in Fig. 9. The temperature distribution is depicted using a color gradient, with the red regions indicating higher temperatures compared to the blue regions, and the black curves indicate lines of equal temperature. Fig. 9(a) shows the temperature distribution within a depth of up to 2 μm over a time span of 8 to 30 ns. It is observed that upon laser pulse injection onto the material, the temperature at target surface rapidly exceeds 10,000 K within 5 ns. This high temperature surpasses the ablation threshold of Al, leading to an immediately evaporation-induced ablation. Subsequently, the temperature gradually decreases at a slow rate. Considering that the boiling point of the target material (Al) is approximately 2730

K, the evaporation-induced ablation depth can be calculated based on the surface temperature history using the Hertz-Knudsen equation. Fig. 9(b) shows the temperature evolution over a time range of 30 to 300 ns and a depth of up to 20 μm. The thermal relaxation time is considerably longer than the 5 ns pulse duration. Based on the modeling results, the temperature remains above 1000 K for approximately 300 ns, providing sufficient time and a stable condition for the occurrence of ultrafast chemical reactions.

To thoroughly investigate the contribution of high-temperature-induced ultrafast chemical reaction to the material removal during CE-PLM, simulations are performed under varying processing parameters including laser intensity and number of laser shots. Fig. 10(a) presents the results from single-shot laser ablation under different confining media. Since the high-temperature time span for chemical etching is much longer than that for the evaporation during laser ablation of Al according to Fig. 9, it is reasonable to estimate the contribution of chemical etching to the ablation depth by subtracting the evaporation-induced depth from the total depth. It is found that the contribution of chemical etching to the material removal gradually increases with

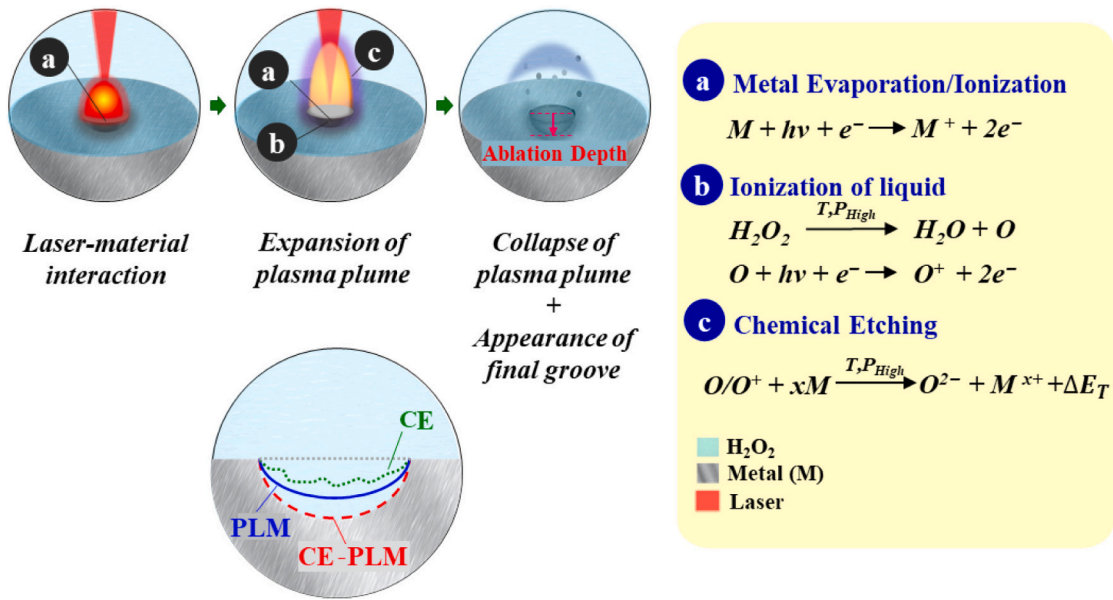


Fig. 8. The schematic representation of the CE-PLM process mechanism.

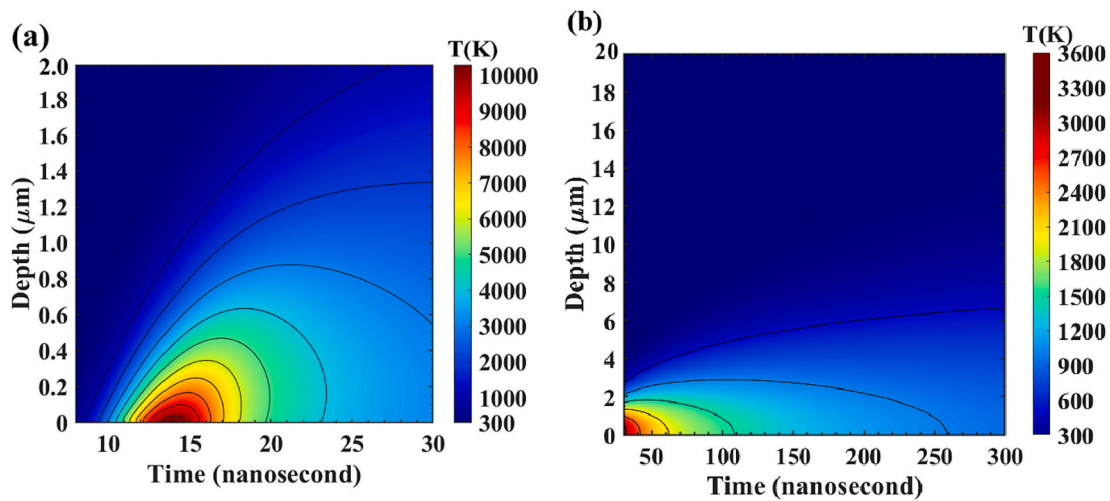


Fig. 9. Simulated spatial-temporal evolution of temperature for the laser ablation of Al: (a) 8–30 ns and 0–2 μm, (b) 30–300 ns and 0–20 μm.

increasing the laser intensity. For example, given a laser intensity of 7 GW/cm², the evaporation and chemical etching contribute 64.2% (5.36 μm in depth) and 35.8% (2.99 μm in depth) to the total ablation, respectively. When increasing the laser intensity to 15 GW/cm², the material removal contributed from evaporation decreases to 50.3% (7.37 μm in depth) whereas that from chemical etching increases to 49.7% (7.28 μm in depth). This observation can be elucidated by the following explanation. When the laser intensity increases, the peak temperature increases, accompanied by the prolonged thermal relaxation time, contributing to a faster and longer etching process and thus exponentially increasing the material removal caused by chemical reaction. Such prediction regarding the ablation depth as affected by laser intensity quantitatively aligns well with the experimental data. In addition, by incorporating the Gaussian energy distribution in a transverse plane, the cross-sectional profiles of the crater after laser ablation can be derived according to the calculated total depth. As observed in Fig. 10(b), the modeling outcomes also exhibit a satisfactory agreement with the experimental data, providing further evidence of the model's efficacy in predicting the depth and profile of ablated crater with the consideration of both evaporation and ultrafast chemical etching

reaction.

To further investigate the contribution of chemical etching to the material removal in the practical application, multi-shot PLM modeling is performed and compared with micro-grooving experimental results at a laser intensity of 7 GW/cm², as shown in Fig. 11. Fig. 11(a) demonstrates the groove depth as affected by the scanning times for w-PLM and CE-PLM. The modeling results indicate that the contribution of chemical etching to the material removal gradually decreases with increasing the scanning times, whereas the evaporation demonstrates the opposite trend. For example, given the scanning times of 50, the contribution of evaporation and chemical etching are 53.5% and 46.5%, respectively. By increasing the scanning times to 200, the contribution of evaporation increases to 57.6% while the chemical etching decreases to 42.4%. The predicted trend matches well with the experimental measurements and can be explained as follows. With the increase of scanning times, the micro-grooves become deeper, leading to the increased distance between the focal plane of the laser beam and the target surface and consequently decreased laser intensity. This is supported by calculating the ablation rate shown in the inset figure. However, since the micro-grooves produced by CE-PLM is much deeper than that produced by

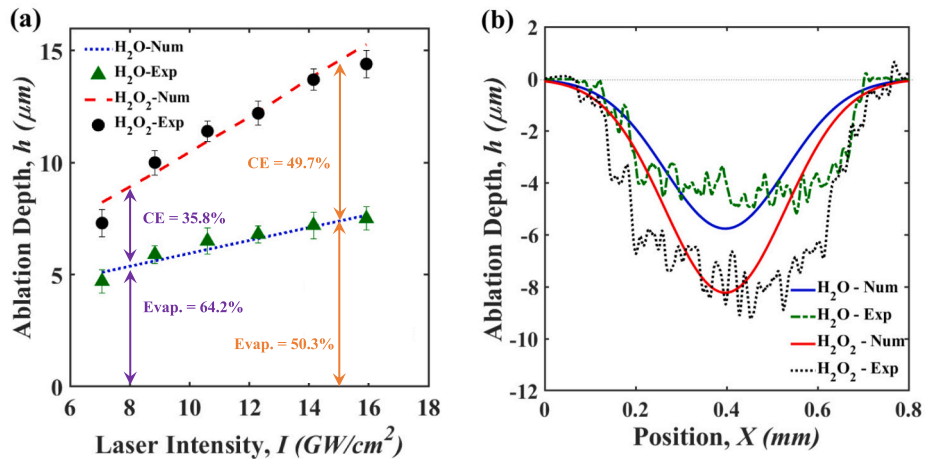


Fig. 10. (a) Comparison between experimental data and modeling results for the ablation depths of Al achieved under H_2O_2 and H_2O with varying laser intensities. (b) Comparison between experimental data and modeling results for the cross-sectional profiles processed by laser ablation under H_2O and H_2O_2 , with a laser intensity of $7 \text{ GW}/\text{cm}^2$.

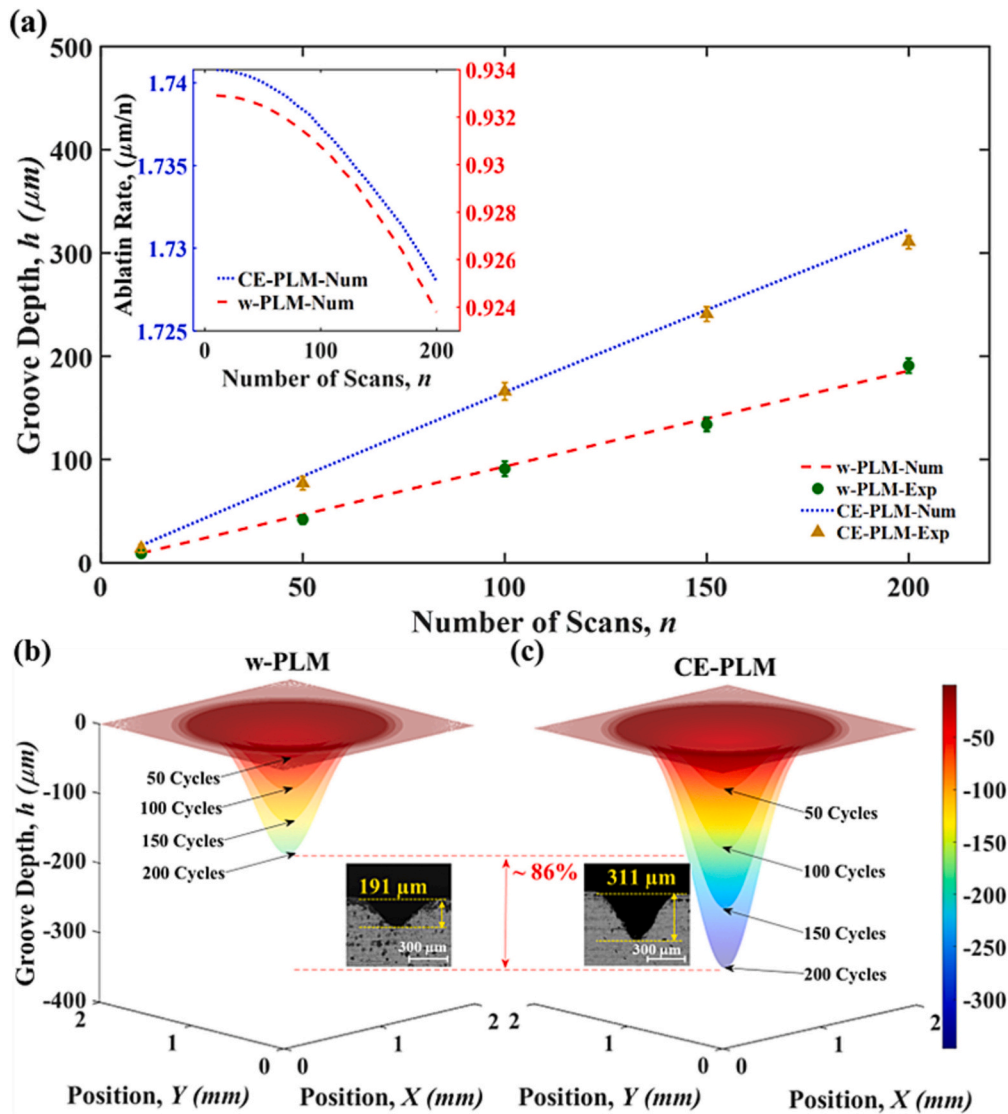


Fig. 11. (a) Comparison of ablation depth of Al for scanning times from 10 to 200 proceed by w-PLM and CE-PLM process using the laser intensity of $7 \text{ GW}/\text{cm}^2$, and 3D plots of shape of crater formed by (b) w-PLM and (c) CE-PLM process at various scanning numbers.

w-PLM with the same energy input, the decrease in effective laser intensity becomes more significant for CE-PLM, which further reduces the contribution of etching reaction to the material removal. The decreased contribution of chemical etching due to the decreased laser intensity could be addressed by maintaining the distance between focal plane and target recession surface (e.g., percussion drilling). Fig. 11(b, c) presents pseudo 3D representations of the ablated region obtained using the calculated depth and a 3D coordinate system based on a Gaussian laser shape to provide insight into the PLM process by visualizing the shape of the ablated region. The cross-sectional view of the 3D profile demonstrates a distinct “V-shape” morphology, and its dimensions match well with the SEM imaging results. According to the above results, one can conclude that the established numerical model has demonstrated its capability of quantitatively predicting the proposed CE-PLM process regarding micromachining efficiency and morphology of ablated region, which could facilitate our understanding in the process mechanism and optimization.

4. Conclusion

In the current work, a high-efficiency and environmentally friendly laser-based micromachining process, CE-PLM, was developed by applying active liquid confinement - H_2O_2 during conventional PLM. The effects of H_2O_2 on the enhanced laser ablation rate and PLM efficiency were evaluated. The underlying mechanism responsible for such enhancements was proposed. Moreover, a physics-based model was established to further elucidate the process mechanism, with focus on revealing the contributions of high-temperature-induced evaporation and etching reaction to the material removal. The modeling results were validated by experimental measurements regarding the as-produced feature profile and depth. According to the experimental and numerical efforts, the major conclusions can be summarized below:

- (1) The single-shot laser ablation experiments demonstrate that as compared to conventional w-PLM, CE-PLM under H_2O_2 exhibits significantly improvement in the ablation rate for various metallic materials including Zn, Al and Cu. When approaching the saturation point, the ablation rate was increased by 156% for Zn at 2.2 GW/cm², 90.2% for Al at 14.15 GW/cm², and 57% for Cu at 11.94 GW/cm². More importantly, CE-PLM overcomes the current major limitation (saturated ablation rate) in w-PLM caused by the plasma screening effect and enables high ablation rates even at high laser intensities.
- (2) The beneficial effect of H_2O_2 on the ablation rate is also extended to practical applications such as micro-drilling and micro-grooving, confirming the substantial improvement in PLM efficiency. For example, given a laser intensity of 7 GW/cm², the number of pulses required to drill a through-hole on a 1-mm-thick Al sheet was decreased by a factor of 7.42, and the microgroove depth produced on the Al sheet was increased by 83.3% at the scanning times of 50. The enhanced ablation rate and process efficiency in CE-PLM can be attributed to the synergistic effect of high-temperature-induced evaporation and localized ultrafast chemical etching reaction.
- (3) With increasing the laser intensity, the contribution of etching reaction to the material removal increases, while the contribution of evaporation decreases. For instance, when increasing the laser intensity from 7 to 15 GW/cm² for processing Al, the contribution of evaporation to the material removal was decreased from 64.2% to 50.3%, whereas the contribution from chemical etching was increased from 35.8% to 49.7%. This is caused by the increased peak temperature and prolonged thermal relaxation time at higher laser intensities, resulting in a faster and longer etching process and thus exponentially increasing the material removal caused by etching reaction.
- (4) For multi-shot PLM applications like micro-grooving, the contribution of chemical etching to the material removal gradually decreases with increasing the scanning times, whereas the evaporation demonstrates the opposite trend. This can be elucidated by the observation that the enhanced material removal by CE-PLM results in deeper micro-grooves, contributing to a greater decrease in effective laser intensity injected onto the recessed material surface mainly caused by the increased distance between the focal plane of the laser beam and target surface.

This study demonstrates the great potential of the developed CE-PLM in improving process efficiency and capability of various PLM techniques. We envision that the findings in the present work could provide valuable insights for CE-PLM process design, control and optimization, enabling its broader industrial applications.

Declaration of competing interest

The authors declare that they have no known competing financial interests or personal relationships that could have appeared to influence the work reported in this paper.

Acknowledgement

Y. Liao gratefully thank support from the U. S. National Science Foundation (NSF) (CMMI-1825739). X. Zhang acknowledges the faculty startup support provided by the School of Mechanical and Electrical Engineering at Soochow University.

References

- [1] Teixidor D, Thepsonthi T, Ciurana J, Özel T. Nanosecond pulsed laser micromachining of PMMA-based microfluidic channels. *J Manuf Process* 2012;14:435–42.
- [2] Hwang D, Choi T, Grigoropoulos C. Liquid-assisted femtosecond laser drilling of straight and three-dimensional microchannels in glass. *Appl Phys A* 2004;79:605–12.
- [3] Mao B, Siddaiah A, Menezes PL, Liao Y. Surface texturing by indirect laser shock surface patterning for manipulated friction coefficient. *J Mater Process Technol* 2018;257:227–33.
- [4] Lasemi N, Pacher U, Zhigilei L, Bomati-Miguel O, Lahoz R, Kautek W. Pulsed laser ablation and incubation of nickel, iron and tungsten in liquids and air. *Appl Surf Sci* 2018;433:772–9.
- [5] Xia Y, Jing X, Zhang D, Wang F, Jaffery SHI, Li H. A comparative study of direct laser ablation and laser-induced plasma-assisted ablation on glass surface. *Infrared Phys Technol* 2021;115:103737.
- [6] Sugioka K. Hybrid femtosecond laser three-dimensional micro- and nanoprocessing: a review. *Int J Extreme Manuf* 2019;1:012003.
- [7] Liu X, Du D, Mourou G. Laser ablation and micromachining with ultrashort laser pulses. *IEEE J Quantum Electron* 1997;33:1706–16.
- [8] Zhu S, Lu Y, Hong M, Chen X. Laser ablation of solid substrates in water and ambient air. *J Appl Phys* 2001;89:2400–3.
- [9] Lv J, Dong X, Wang K, Duan W, Fan Z, Mei X. Study on process and mechanism of laser drilling in water and air. *Int J Adv Manuf Technol* 2016;86:1443–51.
- [10] Kang HW, Lee H, Welch AJ. Laser ablation in a liquid-confined environment using a nanosecond laser pulse. *J Appl Phys* 2008;103:083101.
- [11] Shaheen M, Gagnon J, Fryer B. Femtosecond laser ablation of brass in air and liquid media. *J Appl Phys* 2013;113:213106.
- [12] Zhang D, Ranjan B, Tanaka T, Sugioka K. Underwater persistent bubble-assisted femtosecond laser ablation for hierarchical micro/nanostructuring. *Int J Extreme Manuf* 2020;2:015001.
- [13] Yocom CJ, Zhang X, Liao Y. Research and development status of laser peen forming: a review. *Opt Laser Technol* 2018;108:32–45.
- [14] Liu P, Cui H, Wang C, Yang G. From nanocrystal synthesis to functional nanostructure fabrication: laser ablation in liquid. *Phys Chem Chem Phys* 2010;12:3942–52.
- [15] Zhang C, Dong Y, Ye C. Recent developments and novel applications of laser shock peening: a review. *Adv Eng Mater* 2021;23:2001216.
- [16] Wang R, Xu S, Yue Y, Wang X. Thermal behavior of materials in laser-assisted extreme manufacturing: Raman-based novel characterization. *Int J Extreme Manuf* 2020;2:032004.
- [17] Zhang X, Sun H, Mao B, Dai R, Zhuang H, Liao Y, et al. Nanosecond laser shock detonation of nanodiamonds: from laser-matter interaction to graphite-to-diamond phase transition. *Int J Extreme Manuf* 2022;4:015401.
- [18] Zheng C, Shen H. Ablation mechanism in underwater drilling by an ultrafast laser with pulse energy below the water breakdown threshold. *J Manuf Process* 2022;73:354–63.

- [19] Sollier A, Berthe L, Peyre P, Bartnicki E, Fabbro R. Laser-matter interaction in laser shock processing. In: First international symposium on high-power laser macroprocessing. International Society for Optics and Photonics; 2003. p. 463–8.
- [20] Wu B, Shin YC. Laser pulse transmission through the water breakdown plasma in laser shock peening. *Appl Phys Lett* 2006;88:041116.
- [21] Berthe L, Fabbro R, Peyre P, Bartnicki E. Experimental study of the transmission of breakdown plasma generated during laser shock processing. *Eur Phys J Appl Phys* 1998;3:215–8.
- [22] Berthe L, Fabbro R, Peyre P, Bartnicki E. Wavelength dependent of laser shock-wave generation in the water-confinement regime. *J Appl Phys* 1999;85:7552–5.
- [23] López JML, Bakrania A, Coupland J, Marimuthu S. Droplet assisted laser micromachining of hard ceramics. *J Eur Ceram Soc* 2016;36:2689–94.
- [24] Shiby S, Vasa NJ, Shigeki M. Nanosecond and sub-nanosecond laser-assisted microscribing of Cu thin films in a salt solution. *J Micromanuf* 2021;4:138–46.
- [25] Yoon S-S, Lee YB, Khang D-Y. Etchant wettability in bulk micromachining of Si by metal-assisted chemical etching. *Appl Surf Sci* 2016;370:117–25.
- [26] Ali A, Sundaram M. Drilling of crack free micro holes in glass by chemo-thermal micromachining process. *Precis Eng* 2018;54:33–8.
- [27] Zhan D, Han L, Zhang J, Shi K, Zhou J-Z, Tian Z-W, et al. Confined chemical etching for electrochemical machining with nanoscale accuracy. *Acc Chem Res* 2016;49:2596–604.
- [28] Wang X, Zimmer K, Ehrhardt M, Zhang F, Wang J, Wang P, et al. One-step in-situ low damage etching of SiC/SiC composites by high-temperature chemical-assisted laser processing. *Ceram Int* 2022;48:34472–82.
- [29] Zhang Q, Sun S-F, Zhang F-Y, Wang J, Lv Q-Q, Shao Y, et al. A study on film hole drilling of IN718 superalloy via laser machining combined with high temperature chemical etching. *Int J Adv Manuf Technol* 2020;106:155–62.
- [30] Wang Q, Yao P, Li Y, Jiang L, Xu J, Liang S, et al. Inverted pyramid structure on monocrystalline silicon processed by wet etching after femtosecond laser machining in air and deionized water. *Opt Laser Technol* 2023;157:108647.
- [31] Long J, Eliceiri MH, Wang L, Vangelatos Z, Ouyang Y, Xie X, et al. Capturing the final stage of the collapse of cavitation bubbles generated during nanosecond laser ablation of submerged targets. *Opt Laser Technol* 2021;134:106647.
- [32] Alahmari AM, Ahmed N, Darwish S. Laser beam micro-machining under water immersion. *Int J Adv Manuf Technol* 2016;83:1671–81.
- [33] Bulgakova N, Bulgakov A. Pulsed laser ablation of solids: transition from normal vaporization to phase explosion. *Appl Phys A* 2001;73:199–208.
- [34] Christensen BH, Vestentoft K, Balling P. Short-pulse ablation rates and the two-temperature model. *Appl Surf Sci* 2007;253:6347–52.
- [35] Ivanov DS, Zhigilei LV. Combined atomistic-continuum modeling of short-pulse laser melting and disintegration of metal films. *Phys Rev B* 2003;68:064114.
- [36] Hatef A, Fortin-Deschênes S, Meunier M. Simulation of nanosecond laser-induced thermal dynamics of hollow gold nanoshells for hyperthermia therapy. In: AIP Conf. Proc., AIP; 2014. p. 105–10.
- [37] Zhang Y, Zhang D, Wu J, He Z, Deng X. A thermal model for nanosecond pulsed laser ablation of aluminum. *AIP Adv* 2017;7:075010.
- [38] Lu Q, Mao SS, Mao X, Russo RE. Theory analysis of wavelength dependence of laser-induced phase explosion of silicon. *J Appl Phys* 2008;104:083301.
- [39] Lutey AH. An improved model for nanosecond pulsed laser ablation of metals. *J Appl Phys* 2013;114:083108.
- [40] Mihai State AM, Puscas Niculae N. Pulsed laser ablation of solids, basics, theory and applications. Springer; 2014.
- [41] Farid N, Harilal S, Ding H, Hassanein A. Emission features and expansion dynamics of nanosecond laser ablation plumes at different ambient pressures. *J Appl Phys* 2014;115:033107.
- [42] Hong ZK, Farooq A, Barbour EA, Davidson DF, Hanson RK. Hydrogen peroxide decomposition rate: a shock tube study using tunable laser absorption of H₂O near 2.5 μ m. *J Phys Chem A* 2009;113:12919–25.
- [43] Charee W, Tangwarodomnukun V, Dumkum C. Laser ablation of silicon in water under different flow rates. *Int J Adv Manuf Technol* 2015;78:19–29.
- [44] Wolanov Y, Prikhodchenko PV, Medvedev AG, Pedahzur R, Lev O. Zinc dioxide nanoparticles: a hydrogen peroxide source at moderate pH. *Environ Sci Technol* 2013;47:8769–74.
- [45] Foteinopoulos P, Papacharalampopoulos A, Stavropoulos P. On thermal modeling of additive manufacturing processes. *CIRP J Manuf Sci Technol* 2018;20:66–83.
- [46] Chase MW, N.I.S. Organization. NIST-JANAF thermochemical tables. DC: American Chemical Society Washington; 1998.
- [47] Benavides O, May Ldlc, Gil AF. A comparative study on reflection of nanosecond Nd-YAG laser pulses in ablation of metals in air and in vacuum. *Opt Express* 2013; 21:13068–74.
- [48] Stafe M, Negutu C, Popescu IM. Theoretical determination of the ablation rate of metals in multiple-nanosecond laser pulses irradiation regime. *Appl Surf Sci* 2007; 253:6353–8.
- [49] Stafe M, Marcu A, Puscas NN. Pulsed laser ablation of solids: basics, theory and applications. Springer Science & Business Media; 2013.
- [50] Zhao W, Wang L, Yu Z, Chen J, Yang J. A processing technology of grooves by picosecond ultrashort pulse laser in Ni alloy: enhancing efficiency and quality. *Opt Laser Technol* 2019;111:214–21.
- [51] Mao X, Chan W-T, Caetano M, Shannon MA, Russo RE. Preferential vaporization and plasma shielding during nano-second laser ablation. *Appl Surf Sci* 1996;96: 126–30.